

Measurement of spin pumping voltage separated from extrinsic microwave effects

Ryo Iguchi^{1*} and Eiji Saitoh¹⁻⁵

¹Institute for Materials Research, Tohoku University, Sendai 980-8577, Japan

²WPI Advanced Institute for Materials Research, Tohoku University, Sendai 980-8577, Japan

³Center for Spintronics Research Network, Tohoku University, Sendai 980-8577, Japan

⁴Spin Quantum Rectification Project, ERATO, Japan Science and Technology Agency, Sendai 980-8577, Japan

⁵Advanced Science Research Center, Japan Atomic Energy Agency, Tokai 319-1195, Japan

Abstract

Conversions between spin and charge currents are core technologies in recent spintronics. In this article, we provide methods for estimating inverse spin Hall effects (ISHEs) induced by using microwave-driven spin pumping (SP) as a spin-current generator. ISHE and SP induce an electromotive force at the ferromagnetic or spin-wave resonance, which offers a valuable electric way to study spin physics in materials. At the resonance, a microwave for exciting the magnetization dynamics induces an additional electromotive force via rf-current rectification and thermoelectric effects. We discuss methods to separate the signals generated from such extrinsic microwave effects by controlling sample structures and configurations. These methods are helpful in performing accurate measurements on ISHE induced by SP, enabling quantitative studies on the conversion between spin and charge currents on various kinds of materials.

1 Introduction

Currents of spin angular momentum play a central role in the field of spintronics. Significant contributions have been made by spin currents, such as control of magnetizations by spin transfer torque,[1–4] transmission of electric signals through insulators,[5–

*iguchi@imr.tohoku.ac.jp

7] thermoelectric conversion,[8–12] and electric probing of insulator magnetization.[13–15] In order to detect and utilize these spin based-phenomena, conversion between spin and charge currents is necessary. For realizing efficient spin-to-charge current conversion, a wide range of materials are currently being investigated, including metals,[16–25] semiconductors,[26–32] organic materials,[33, 34] carbon-based materials,[35] and topological insulators.[36–38] Finding materials suitable to the spin-to-charge conversion is thus indispensable to making spintronic devices.

One of the popular methods of the spin-to-charge conversion is the inverse spin Hall effect (ISHE),[16, 25] which is the reciprocal effect of the spin Hall effect[27, 28, 31, 39] caused by spin-orbit interaction. In the ISHE, a spin current generates a transverse charge current in a conductor such as Pt. Since the first demonstration of the ISHE in Pt and Al,[16, 22] it has been extensively studied because of its versatility.[40, 41]

Dynamical generation of spin currents can be achieved by the spin pumping (SP).[42–44] At the interface between a normal conductor (N) and a ferromagnet (F), the SP causes emission of spin currents into the N layer from magnetization dynamics in the adjacent F layer. Such the magnetization dynamics is typically triggered by applying a microwave field; at the ferromagnetic resonance (FMR) or the spin wave resonance (SWR) condition, the magnetization resonantly absorbs the microwave power and exhibits a coherent precessional motion. A part of the angular momenta stored in this precessional motion is the source of the spin current generated by the SP.

The combination of the ISHE and the SP enables electric detection and generation of spin currents.[16, 25] This is the setup commonly used to study the properties of spin-to-charge current conversion and spin transport in materials. A spin current is injected into an N layer by the SP and is converted to a measurable electromotive force by the ISHE. The conversion efficiency between spin and charge currents in this process can be determined by estimating the density of the injected spin current by analyzing microwave spectra.[20, 45] The spin transport property of a material can be investigated by constructing a heterostructure in which the material of interest is placed between a spin-current injector and detector layers.[35, 46, 47]

It should be noted that the voltage signal from the ISHE can be contaminated by other contributions in practice experiments. We thus need to extract the ISHE contribution by separating or minimizing the unwanted signals in order to ensure the validity of the measurements.[20, 32, 48–51] The ISHE signal is characterized by Lorentzian spectral shape and sign change under the magnetization reversal,[45] and some of the unwanted signals show the same spectral shape and the sign change in configurations commonly used in the SP experiments.[32, 52] Such signals can be induced by a temperature gradient via thermoelectric effects[36, 53–55] and by an rf current via rectification effects (See Fig. 1).[56–59] The heat emitted by excited magnetization dynamics induces a thermal gradient in a sample, resulting in an electromotive force due to the conventional Seebeck effect. This type of heat induced signals can be eliminated if one designs experimental conditions appropriately. Rectification effects comes from interplay between stray rf currents induced by an incident microwave and galvanomagnetic effects coming from oscillating magnetizations. The direction, magnitude, and phase of the stray rf current contain uncertainty because they depend on the details of an experimental setting, so the signals from the rectification effects tend to be complicated. Since the rectification effects were first observed in 1963 in a Ni film with the

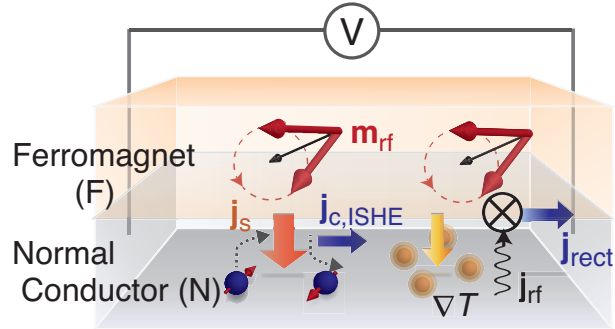


Fig. 1: (Color online) A schematic illustration of the SP and ISHE processes. The SP induces an spin current, \mathbf{j}_s , and the ISHE convert \mathbf{j}_s into an charge current, $\mathbf{j}_{c, \text{ISHE}}$. A microwave driving the FMR induces an rf current, \mathbf{j}_{rf} , causing a dc current j_{rect} via galvanomagnetic effects. The absorbed microwave power at FMR induces a temperature gradient, ∇T , causing a thermoelectric voltage. These process results in unwanted signals.

anisotropic magnetoresistance (AMR) and the anomalous Hall effect (AHE),[56] we can not make light of the effects. A number of works regarding to the extraction of the ISHE signal from other contributions in electric measurements on the SP have been reported.[20, 32, 48–51]

In this article, we review the previous studies of the voltage signals induced by the SP and further introduce some methods to analyze the signals on the FMR. Here, we will focus on the experiments in a microwave cavity, so that small density of induced rf currents and thus small rectification contribution can be expected. The original field distribution in a cavity is minimally disturbed by placing a sample in it because the empty region in the cavity does not carry rf currents. In experiments, it is often difficult to identify the origin of the stray rf currents because it depends on an individual setup: the sample structure including wires for electric measurements. In this paper, we describe methods to separate the SP contribution from other artifacts in the electric measurements by introducing parameter dependence to the voltages in the presence of the stray rf currents. The methods can be applied to systems with a microstrip line or coplanar waveguide, but the rf-current-induced magnetization excitation due to the SHE, or the spin transfer torque FMR (STT-FMR), [60, 61] is neglected.

This article is organized as follows. In Section 2, we show the analytical descriptions of the signals from the SP, rectification effects, and heating effects based on the magneto-circuit theory[43] and the Landau-Lifshitz-Gilbert (LLG) equation[62]. In Section 3, we discuss the dependence of the signals on the FMR spectrum, sample geometry, magnetization orientation, and excitation frequency. Here, we point out the similarity between the voltage signals due to the SP and rectification effects. Finally, in Section 4, we give a summary of the methods based on the dependences described in Section 3 and emphasize that the voltage measurement of the in-plane magnetization angular dependence with out-of-plane microwave magnetic field in a properly designed

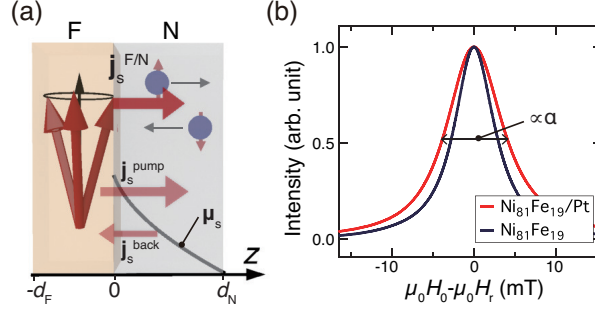


Fig. 2: (Color online) (a) F/N bilayer system under the SP. F (N) denotes the ferromagnet (normal conductor) layer. (b) Normalized FMR spectra of $\text{Ni}_{81}\text{Fe}_{19}$ and $\text{Ni}_{81}\text{Fe}_{19}/\text{Pt}$ systems, where H_0 denotes the strength of an applied field and H_r denotes the FMR field.

system is the most reliable way and thus enables quantitative studies of the SP on various kinds of materials.

2 Signals due to spin pumping and microwave effects in bilayer systems

In this section, we discuss the analysis of the voltage signals induced by the SP, rectification effects, and heating effects. For the calculation of the SP-induced ISHE signal, we consider a spin current generated by magnetization dynamics via the SP in a bilayer film consisting of a normal conductor (N) and a ferromagnet (F). The rectification signals are expressed using the derived magnetization dynamics for the SP. For the heating-induced signals, we discuss thermoelectric effects due to the heating at the FMR and SWR of magnetostatic surface spin waves.

2.1 Spin current induced by spin pumping

The spin pumping (SP) is the phenomenon that a magnetically excited F layer induces a spin current into the N layer placed adjacent to it.[42, 44] Here, let us suppose the N and the F layers span xy plane, and they are stacked in z direction [Fig. 2(a)]. The spin current density through the F/N interface due to the SP is given by[43]

$$\mathbf{j}_s^{\text{pump}} = \frac{\hbar}{4\pi} g_r^{\uparrow\downarrow} (\mathbf{m} \times \dot{\mathbf{m}}) + \frac{\hbar}{4\pi} g_i^{\uparrow\downarrow} \dot{\mathbf{m}}, \quad (1)$$

where \mathbf{m} denotes the unit vector along the magnetization in the F layer, $\dot{\mathbf{m}}$ the time derivative of \mathbf{m} , and $g_r^{\uparrow\downarrow}$ ($g_i^{\uparrow\downarrow}$) the real (imaginary) part of mixing conductance per unit area, \hbar the Planck constant. The spin polarization of $\mathbf{j}_s^{\text{pump}}$ is represented by its vector direction, and its flow direction is the interface normal \mathbf{z} . In diffusive N layers, the spin accumulation μ_s is formed owing to the pumped spin current. This spin accumulation

induces a back-flow spin current into the F layer, and it renormalizes the mixing conductance in Eq. (1) to an effective one denoted by $g_{\text{eff}}^{\uparrow\downarrow}$. The back-flow spin current density from the magneto-circuit theory is given by[43]

$$\mathbf{j}_s^{\text{back}} = \frac{1}{4\pi} g_r^{\uparrow\downarrow} \mathbf{m} \times (\boldsymbol{\mu}_s^{\text{F/N}} \times \mathbf{m}) + \frac{1}{4\pi} g_i^{\uparrow\downarrow} \boldsymbol{\mu}_s^{\text{F/N}} \times \mathbf{m} \quad (2)$$

when the spin relaxation is fast enough and $\boldsymbol{\mu}_s^{\text{F/N}} \propto \mathbf{j}_s^{\text{pump}}$ holds,[63] where $\boldsymbol{\mu}_s^{\text{F/N}}$ denotes the spin accumulation at the F/N interface ($z = 0$). The solution without the approximation can be found in Ref. 63. Then, combining Eqs. (1) and (2), one can find the net dc spin current density,

$$\mathbf{j}_s^{\text{F/N}} = \mathbf{j}_s^{\text{pump}} - \mathbf{j}_s^{\text{back}} = \frac{\hbar}{4\pi} g_{r,\text{eff}}^{\uparrow\downarrow} \mathbf{m} \times \dot{\mathbf{m}} + \frac{\hbar}{4\pi} g_{i,\text{eff}}^{\uparrow\downarrow} \dot{\mathbf{m}}, \quad (3)$$

where $g_{r(i),\text{eff}}^{\uparrow\downarrow}$ represents the real (imaginary) part of the effective mixing conductance per unit area. The mixing conductance at the F/N interfaces has been widely investigated in many combinations of materials.[64–66] Hereafter $g_{i,\text{eff}}^{\uparrow\downarrow}$ is omitted for simplicity because it is much smaller than the real part.[67, 68]

The expression of $g_{r,\text{eff}}^{\uparrow\downarrow}$ can be obtained in terms of the parameters of the N layer. $\boldsymbol{\mu}_s^{\text{F/N}}$ is calculated from the spin accumulation profile $\boldsymbol{\mu}_s(z)$ determined by the spin diffusion equation[63]

$$\frac{\partial}{\partial t} \boldsymbol{\mu}_s(z) = -\gamma_N \boldsymbol{\mu}_s(z) \times \mu_0 \mathbf{H}_0 + D \nabla^2 \boldsymbol{\mu}_s(z) - \frac{\boldsymbol{\mu}_s(z)}{\tau_s} \quad (4)$$

with the boundary conditions: $-\frac{\hbar\sigma_N}{4e^2} \nabla \boldsymbol{\mu}_s(0) = \mathbf{j}_s^{\text{F/N}}$ at the interface ($z = 0$) and $-\frac{\hbar\sigma_N}{4e^2} \nabla \boldsymbol{\mu}_s(d_N) = 0$ at the outer boundary of the N layer ($z = d_N$). $\sigma_{\text{N(F)}}$ and $d_{\text{N(F)}}$ are the conductivity and thickness of the N (F) layer. γ_N denotes the gyromagnetic ratio of electrons in the N layer, e the electron charge, μ_0 the permittivity of a vacuum, \mathbf{H}_0 an external field, D the diffusion constant, and τ_s the spin-relaxation time. We focus on the regime where the Hanle effect is negligibly small (a rigorous treatment can be found in Ref. 29). Then, $\boldsymbol{\mu}_s(z)$ is obtained as

$$\boldsymbol{\mu}_s(z) = \frac{4e^2}{\hbar\sigma_N} \lambda \frac{\cosh[(z - d_N)/\lambda]}{\sinh(d_N/\lambda)} \mathbf{j}_s^{\text{F/N}}, \quad (5)$$

where $\lambda \equiv \sqrt{D\tau_s}$ denotes the spin diffusion length. Using Eqs. (2), (3), and (5), we find that the effective mixing conductance is given by

$$g_{r,\text{eff}}^{\uparrow\downarrow} = \left(\frac{1}{g_r} + \frac{\pi\hbar\sigma_N}{e^2\lambda} \tanh \frac{d_N}{\lambda} \right)^{-1}. \quad (6)$$

2.2 Magnetization dynamics and spin current

Next, let us examine the effect of the SP on magnetization dynamics. We will calculate the effective mixing conductance and the magnitude of a pumped spin current in terms of observable parameters in experiments.

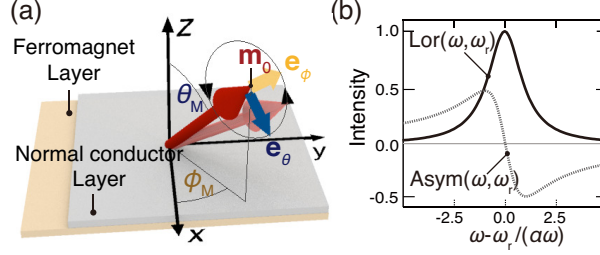


Fig. 3: (Color online) (a) Spatial coordinate of the system, where \mathbf{m}_0 denotes unit vector in the direction of the equilibrium magnetization and is identical with \mathbf{e}_r . (b) Spectral shapes of $\text{Lor}(\omega, \omega_r)$ and $\text{Asym}(\omega, \omega_r)$.

The SP affects magnetization dynamics. When the incoming and outgoing spin currents, given by $\gamma \text{div}(\mathbf{j}_s^{\text{F/N}}) / (d_F I_s)$, are included, the LLG equation[62] is modified as

$$\begin{aligned} \dot{\mathbf{m}} = & -\gamma \mathbf{m} \times \mu_0 [\mathbf{H}_{\text{eff}}(\mathbf{m}) + \mathbf{h}_{\text{rf}}(t)] \\ & + \left(\alpha_0 + \frac{\gamma}{d_F I_s} \frac{\hbar}{4\pi} g_{\text{r,eff}}^{\uparrow\downarrow} \right) \mathbf{m} \times \dot{\mathbf{m}} \end{aligned} \quad (7)$$

where γ denotes the gyromagnetic ratio of the ferromagnet F, $\mathbf{H}_{\text{eff}}(\mathbf{m})$ the effective field, $\mathbf{h}_{\text{rf}}(t)$ an microwave field, α_0 the Gilbert damping constant without spin current exchange, and I_s the saturation magnetization. The effective field is given by $\mathbf{H}_{\text{eff}}(\mathbf{m}) = -\nabla_{\mathbf{m}} F_m / I_s$, where the magnetostatic energy F_m includes magnetocrystalline anisotropy. The second term in the second line of Eq. (7) indicates that the SP acts as an additional damping term.[42] The reverse process is also demonstrated; a spin current injected from the N layer reduces the damping of the F layer.[69]

Finding the enhanced damping thus directly relates to $g_{\text{r,eff}}^{\uparrow\downarrow}$. In practical experiments, the total damping term represented by $\alpha \mathbf{m} \times \dot{\mathbf{m}}$ is observed. By measuring α from the FMR spectra of F/N and F films,[42, 70] the change in the Gilbert damping constant can be found, i.e. $\Delta\alpha = \alpha_{\text{F/N}} - \alpha_{\text{F}}$. Figure 2(b) shows an example of the comparison of the FMR microwave spectrum for $\text{Ni}_{81}\text{Fe}_{19}/\text{Pt}$ (F/N) bilayer and $\text{Ni}_{81}\text{Fe}_{19}$ (F) single-layer samples, where broadening of the F/N spectral peak can be seen. By fitting the spectral peak using Lorentzian, α is obtained from the full-width at the half-maximum (FWHM) which has the relation $\Delta H = (\partial\omega_r / \partial H_0)^{-1} \alpha (\omega_\theta + \omega_\phi)$ for field strength H_0 swept measurements,[42] where ω and ω_r respectively denote the angular frequency of the magnetization precession and that at the resonance determined by ω_θ and ω_ϕ derived below. Finding the value of $\Delta\alpha$, one obtains

$$g_{\text{r,eff}}^{\uparrow\downarrow} = 4\pi \frac{I_s}{\gamma \hbar} \Delta\alpha d_F. \quad (8)$$

The measurement of $\Delta\alpha$ requires some care. Since the magnetic properties of a ferromagnetic film in a heterostructure are affected by the other part of the structure,[71]

there can be contributions on $\Delta\alpha$ other than the SP through inhomogeneous broadening and two-magnon scattering. Thus careful comparison of α is required.[42, 72, 73]

In order to find the spectral shape and magnitude of the spin current $\mathbf{j}_s^{F/N}$, we calculate the magnetization dynamics $\mathbf{m} \times \dot{\mathbf{m}}$ from Eq. (7). Here, we consider precessing magnetization $\mathbf{m}_{\text{rf}} \equiv \text{Re} \left[(m_\theta \mathbf{e}_\theta + m_\phi \mathbf{e}_\phi) \exp(i\omega t) \right]$ around the equilibrium magnetization vector \mathbf{m}_0 excited by an microwave field $\mathbf{h}_{\text{rf}} \equiv \text{Re} \left[(h_\theta \mathbf{e}_\theta + h_\phi \mathbf{e}_\phi) \exp(i\omega t) \right]$ as shown in Fig. 3. \mathbf{m}_0 is determined by the condition $\mathbf{m}_0 \times \mathbf{H}_{\text{eff}} = 0$. The unit vectors of the polar coordinate \mathbf{e}_p ($p = r, \theta, \phi$) in which \mathbf{e}_r points \mathbf{m}_0 have a relation to the unit vectors of the Cartesian coordinate \mathbf{e}_i ($i = x, y, z$), $\mathbf{e}_p = \sum_{i=x,y,z} u_{pi} \mathbf{e}_i$ with

$$u = \begin{pmatrix} \sin \theta_M \cos \phi_M & \sin \theta_M \sin \phi_M & \cos \theta_M \\ \cos \theta_M \cos \phi_M & \cos \theta_M \sin \phi_M & -\sin \theta_M \\ -\sin \phi_M & \cos \phi_M & 0 \end{pmatrix}, \quad (9)$$

where θ_M and ϕ_M denote the polar angle between the z axis and \mathbf{m}_0 , and the azimuthal angle measured from the x axis, respectively. Taking the time average of the pumped spin current in Eq. (3) yields

$$\langle \mathbf{j}_s^{F/N} \rangle_t = \frac{\hbar\omega}{4\pi} g_{r,\text{eff}}^{\uparrow\downarrow} \text{Im} [m_\theta m_\phi^*] \mathbf{m}_0, \quad (10)$$

where $\langle \dots \rangle_t$ and a^* mean temporal average and complex conjugate of a , respectively. The relation between the magnitude of \mathbf{m}_{rf} and \mathbf{h}_{rf} obtained from the Eq. (7) is reduced to $(m_\theta, m_\phi) = \chi \cdot (h_\theta, h_\phi)$, where the susceptibility χ is given by[74]

$$\chi \approx \frac{\gamma\mu_0}{\alpha\omega} \frac{S(\omega, \omega_r)}{\omega_\theta + \omega_\phi} \begin{pmatrix} \omega_\theta & -\omega_{\theta\phi} + i\omega \\ -\omega_{\theta\phi} - i\omega & \omega_\phi \end{pmatrix} \quad (11)$$

with $\omega_\theta \equiv \omega_{\phi\phi} - \frac{\partial}{\partial m_r} F_m$, $\omega_\phi \equiv \omega_{\theta\theta} - \frac{\partial}{\partial m_r} F_m$, and

$$\omega_{pq} \equiv \frac{\gamma\mu_0}{I_s} \frac{\partial}{\partial m_p} \frac{\partial}{\partial m_q} F_m \quad (p, q \in \{\theta, \phi\}). \quad (12)$$

$S(\omega, \omega_r)$ represents a spectrum function,

$$S(\omega, \omega_r) \equiv \frac{\alpha\omega}{(\omega_r - \omega)^2 + (\alpha\omega)^2} [(\omega_r - \omega) - i\alpha\omega], \quad (13)$$

which real part represents asymmetric spectrum, $\text{Asym}(\omega, \omega_r) \equiv \text{Re} [S(\omega, \omega_r)]$ (known as asymmetric Lorentzian), and which imaginary part represents symmetric spectrum, $\text{Lor}(\omega, \omega_r) \equiv \text{Im} [S(\omega, \omega_r)]$ (Lorentzian). The resonance angular frequency ω_r is given by

$$\omega_r \equiv \sqrt{\omega_\theta\omega_\phi - \omega_{\theta\phi}^2}. \quad (14)$$

Calculation using Eq. (11) yields

$$\langle \mathbf{j}_s^{F/N} \rangle_t = \frac{\hbar g_{r,\text{eff}}^{\uparrow\downarrow} \gamma^2 \mu_0^2}{4\pi} \frac{\left(\omega_\theta |h_\theta|^2 + \omega_\phi |h_\phi|^2 + \text{Im} \left[h_\theta h_\phi^* \left\{ \omega_\theta\omega_\phi - (\omega_{\theta\phi} + i\omega)^2 \right\} / \omega \right] \right)}{\alpha^2 (\omega_\theta + \omega_\phi)^2} \text{Lor}(\omega, \omega_r) \mathbf{m}_0, \quad (15)$$

where we used a relation, $|S(\omega, \omega_r)|^2 = \text{Lor}(\omega, \omega_r)$. Equation (15) means that the spectral shape of $\langle \mathbf{j}_s^{\text{F/N}} \rangle_t$ is Lorentzian.[16] Equation (15) can be also expected in terms of the elliptic precession with the cone angle Θ in Refs. 20, 75, 76: at resonance $\mathbf{m}_{\text{rf}} = \text{Re}[\sin \Theta \exp(i\omega t) \mathbf{e}_\theta + iA \sin \Theta \exp(i\omega t) \mathbf{e}_\phi]$ and thus $\text{Im}[m_\theta m_\phi^*] = A \sin^2 \Theta$, where A is a correction factor for the elliptical precession motion.

The magnetization excitation leads to decreased power of the incident microwave and thus microwave measurements are useful for determining α and other parameters related to the resonance condition. The microwave power absorption on the FMR per unit volume is calculated by

$$\begin{aligned} \Delta P &= -\frac{\omega}{2\pi} \int_0^{\frac{2\pi}{\omega}} \mathbf{h} \cdot \mathbf{m} dt \\ &= \frac{\gamma\mu_0}{2} \frac{(\omega_\theta |h_\theta|^2 + \omega_\phi |h_\phi|^2 - 2\text{Re}[h_\theta h_\phi^* (\omega_{\theta\phi} + i\omega)])}{\alpha(\omega_\theta + \omega_\phi)} \text{Lor}(\omega, \omega_r). \end{aligned} \quad (16)$$

The transferred energy from the microwave to the magnetization dynamics finally results in heat via damping processes of the dynamics, which causes thermoelectric signals.

In this calculation, we assumed that \mathbf{h}_{rf} is only induced by an applied microwave field and is not affected by an induced rf current. Rf currents are known to trigger the FMR through generation of rf spin currents via the SHE.[61] This contribution can be included to \mathbf{h}_{rf} by calculating the spin-transfer torque due to the absorption of the rf spin current.[60, 61] Such a contribution will result in a phase shift between the actual rf current and the rf current determined by the analysis provided in this article.

2.3 Voltage generated by inverse spin Hall effect

Here, we describe the electromotive force generated by the SP and ISHE in the N layer by taking account of the spin current profile in the N layer.

The pumped spin current in the N layer gives rise to an electromotive force due to the ISHE. The ISHE induces a charge current density transverse to both the spin polarization ($\propto \mathbf{j}_s$) and its flow direction ($\propto \mathbf{z}$), which can be expressed as[45]

$$\mathbf{j}_{\text{c,ISHE}} = \frac{2e}{\hbar} \theta_{\text{SHE}} \mathbf{j}_s \times \mathbf{z}. \quad (17)$$

Therefore, as $\langle \mathbf{j}_s^{\text{F/N}} \rangle_t \propto \mathbf{m}_0$ holds in the SP, the direction of the ISHE current is reversed under the magnetization reversal ($\mathbf{m}_0 \rightarrow -\mathbf{m}_0$), which is an important feature of the ISHE induced by the SP.

According to the short circuit model,[77] the electromotive force is calculated by the sum of the induced current. The total dc current induced by the ISHE is given by

$$\mathbf{J}_{\text{ISHE}} = w \frac{2e}{\hbar} \theta_{\text{SHE}} \int_0^{d_N} \mathbf{z} \times \langle \mathbf{j}_s(z) \rangle_t dz \quad (18)$$

with w being the width of a sample [See Fig. 4(a)]. One can observe the electromotive force \mathbf{E}_{ISHE} induced by \mathbf{J}_{ISHE} , which satisfies the relation $\tilde{\mathbf{R}}_{\text{tot}} \mathbf{J}_{\text{ISHE}} + \mathbf{E}_{\text{ISHE}} = 0$ for an

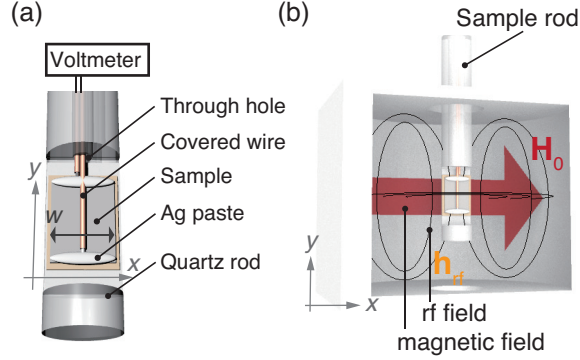


Fig. 4: (Color online) (a) Typical configuration of sample setup for the ISHE measurement by using the SP. (b) Schematic illustration of experimental configuration in a cavity.

open circuit condition, where \tilde{R}_{tot} is the total resistance per unit length of the system, e.g. $\tilde{R}_{\text{tot}}^{-1} = w(\sigma_N d_N + \sigma_F d_F)$ for F/N bilayer systems. The spin current profile is obtained from Eqs. (3) and (5) as

$$\mathbf{j}_s(z) = -\frac{\hbar}{2e} \frac{\sigma_N}{2} \nabla \mu_s(z) \quad (19)$$

$$= \mathbf{j}_s^{\text{F/N}} \frac{\sinh([d_N - z]/\lambda)}{\sinh(d_N/\lambda)}. \quad (20)$$

Then we yields

$$\mathbf{E}_{\text{ISHE}} = w \tilde{R}_{\text{tot}} \theta_{\text{SHE}} \frac{2e}{\hbar} \lambda \tanh \frac{d_N}{2\lambda} \langle j_s^{\text{F/N}} \rangle_t \mathbf{z} \times \mathbf{m}_0 \quad (21)$$

from Eqs. (3), (18), and (20).

A typical experimental setup for observing the ISHE voltage is depicted in Fig. 4(b). A bilayer sample is placed on a cutout of a quartz rod, which has a through hole in the center for wires connected to a voltmeter. The wires are covered by an insulating polymer and connected to the electrodes in the y axis. These wires measure the y component of Eq. (21), so that the maximized ISHE voltage is detected when the magnetization points along the x axis. \mathbf{m}_0 is controlled by an applied field, \mathbf{H}_0 . During the measurements, while ω is fixed, the field strength H_0 is swept so that ω_r is changed.

2.4 Voltage generated by rectification effects

Rectification effects at the FMR are caused by an rf current in a sample possessing a galvanomagnetic effect, i.e. magnetization dependent resistivity $\rho(\mathbf{m})$. Describing the resistivity which oscillates due to the precessing magnetization as $\tilde{\rho}(\mathbf{m}) \propto m_p \cos(\omega t)$ and an rf current as $j_{\text{rf}} = j_{\text{rf}}^0 \cos(\omega t + \psi)$, a rectified dc electromotive force, E_{rect} , is

given by

$$\begin{aligned} E_{\text{rect}} &\propto m_p \cos(\omega t) \cdot j_{\text{rf}}^0 \cos(\omega t + \psi) \\ &\propto \frac{j m_p}{2} [\cos \psi + O(t)], \end{aligned} \quad (22)$$

where ψ denotes the phase difference between the precessing magnetization and the rf current, as depicted in Fig. 6(a). Here, we will consider the anisotropic magnetoresistance (AMR), the anomalous Hall effect (AHE), and the spin Hall magnetoresistance (SMR), which are common examples of galvanomagnetic effects in the bilayer systems used in the SP measurements. Note that any effect leading to magnetization dependent resistance gives a dc voltage signal. Therefore the tunnel magnetoresistance,[78–80] the colossal magnetoresistance,[81] and the spin accumulation Hall effect[82] can give the rectified dc voltages which can be calculated in the way described below.

The induced voltage is calculated from the Ohm's law $E_i = \rho_{ij}(\mathbf{m}) j_{\text{rf}}^j$, where j_{rf}^i denotes the i -th component of an rf current passing through a sample.[56] For an F layer with the AMR and AHE, the resistivity tensor can be expanded in terms of the magnetization by

$$\rho_{ij}^{\text{F}}(\mathbf{m}) = \rho_{ij}^0 + \Delta\rho_{\text{AMR}} m_i m_j + \rho_{\text{AHE}} \sum_{l=x,y,z} \epsilon_{ijl} m_l, \quad (23)$$

where m_i denotes the component in the i axis and ϵ denotes the Levi-Civita tensor. ρ_{ij}^0 denotes the resistivity part insensitive to \mathbf{m} , $\Delta\rho_{\text{AMR}}$ the AMR coefficient, and ρ_{AHE} the AHE coefficient. For an N layer with the SMR, whose magnitude is $\Delta\rho_{\text{SMR}}$, the resistivity tensor is given by[83]

$$\rho_{ij}^{\text{N}}(\mathbf{m}) = \rho_{ij}^0 - \Delta\rho_{\text{SMR}} \sum_{k=x,y} \epsilon_{ikz} m_k \sum_{l=x,y} \epsilon_{jly} m_l + \rho_{\text{AHE}}^{\text{N}} \epsilon_{ijz} m_z. \quad (24)$$

Substituting $m_i = \sum_{p=\theta,\phi} u_{pi} m_p$ with u_{pi} in Eq. (9) and extracting the components proportional to precessing magnetization, m_θ and m_ϕ , yields the time-dependent resistivity tensor $\tilde{\rho}^{\text{F(N)}}$ for the F (N) layer [cf. Ref. 50]. Then the i -th component of the rectified dc current density from the j -th component of the rf current is given by $\sigma_{\text{F(N)}} \text{Re} [\tilde{\rho}_{ij}^{\text{F(N)}} j_{\text{rf}}^{j*}] / 2$ for the F(N) layer. Considering the short circuit model, the electromotive force \mathbf{E}_{rect} is obtained as

$$\mathbf{E}_{\text{rect}} = \tilde{R}_{\text{tot}} \left(\int_{-d_{\text{F}}}^0 \frac{\sigma_{\text{F}}}{2} \text{Re} [\tilde{\rho}^{\text{F}} \cdot \mathbf{j}_{\text{rf}}^*(z)] dz + \int_0^{d_{\text{N}}} \frac{\sigma_{\text{N}}}{2} \text{Re} [\tilde{\rho}^{\text{N}} \cdot \mathbf{j}_{\text{rf}}^*(z)] dz \right). \quad (25)$$

An origin of z dependence of $\mathbf{j}_{\text{rf}}(z)$ comes from the skin effect (which appears as the Dyson effect[84] for the microwave resonance experiments). $\mathbf{j}_{\text{rf}}(z)$ is localized within the skin depth: $\delta_{\text{skin}} = 2(\sigma\mu\omega)^{-1/2}$, where μ denotes the permeability. δ_{skin} is typically smaller than the thickness of systems used for the SP experiments; for example, δ_{skin} for Cu at $\omega/2\pi=10$ GHz is estimated to be $0.6 \mu\text{m}$, and the thickness scale used in the experiments is less than a few hundred nanometers.

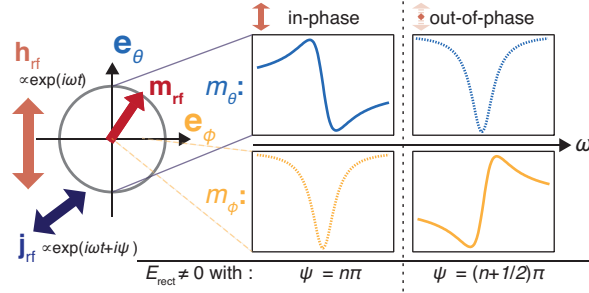


Fig. 5: (Color online) Spectral shapes of the rectification signal E_{rect} induced by m_θ and m_ϕ at $t = 0$ (real part) and $t = \pi / (2\omega)$ (imaginary part). ψ is the phase difference between the rf field $h_{\text{rf}} \exp(i\omega t)$ and the rf current $j_{\text{rf}} \exp(i[\omega t + \psi])$.

The in-plane electromotive force induced by an rf current which lies in the film plane (xy plane) and homogeneous over z is

$$\begin{pmatrix} E_{\text{rect}}^x \\ E_{\text{rect}}^y \end{pmatrix} = \frac{\tilde{R}_{\text{tot}}}{2} \sin \theta_M \sum_{L=F,N} \sigma_L d_L \times \left\{ \left[\cos \theta_M \rho_L^\theta + \rho_{\text{AHE}}^L \begin{pmatrix} 0 & 1 \\ -1 & 0 \end{pmatrix} \right] \text{Re} \left[m_\theta \begin{pmatrix} j_{\text{rf}}^{x*} \\ j_{\text{rf}}^{y*} \end{pmatrix} \right] + \rho_L^\phi \text{Re} \left[m_\phi \begin{pmatrix} j_{\text{rf}}^{x*} \\ j_{\text{rf}}^{y*} \end{pmatrix} \right] \right\} \quad (26)$$

with

$$\rho_{F(N)}^\theta = \Delta \rho_{\text{AMR(SMR)}} \begin{pmatrix} +(-)1 + \cos(2\phi_M) & \sin(2\phi_M) \\ \sin(2\phi_M) & +(-)1 - \cos(2\phi_M) \end{pmatrix}, \quad (27)$$

$$\rho_{F(N)}^\phi = \begin{pmatrix} -\sin(2\phi_M) & \cos(2\phi_M) \\ \cos(2\phi_M) & \sin(2\phi_M) \end{pmatrix}, \quad (28)$$

where $+$ ($-$) sign on the first term of the diagonal parts corresponds to the F (N) layer. The magnitude and spectral shape are determined by $\text{Re} [m_p j_{\text{rf}}^{i*}]$ through Eq. (11). Figure 5 shows possibly induced spectra with various j_{rf}^{i*} in response to the dynamic magnetizations, which exhibits both the Lorentzian and asymmetric Lorentzian. The rectification signals show linear dependence to the incident power because $m_p \propto h_{\text{rf}}$ and $j_{\text{rf}} \propto h_{\text{rf}}$, which is same as the ISHE signal since $\langle j_s^{F/N} \rangle_t \propto \text{Im} [m_\theta m_\phi^*] \propto h_{\text{rf}}^2$.

In the following, we discuss the origin of the stray rf currents causing the extrinsic signals in the previous experiments. One possible origin of the rf current in a cavity is the generation due to the Ohm's law because of a non-zero rf electric field, \mathbf{E}_{rf} , which is considered in most of the previous studies.[16, 32, 45, 48] However, in an open circuit condition, a conductor smaller than the microwave wavelength, typically ~ 1 cm for the X-band microwaves, can screen \mathbf{E}_{rf} below the plasma frequency, which results in a displacement current $\mathbf{j}_{\text{dis}} \approx i\epsilon\omega\mathbf{E}_{\text{rf}}$ rather than the rf current $\mathbf{j}_{\text{rf}} = \sigma\mathbf{E}_{\text{rf}}$ induced by the Ohm's law [See Fig. 6(b)]. Here ϵ is the permittivity. A simulation in Ref. 85 shows that the original cavity field distribution is modified so that \mathbf{E}_{rf} in a conductor is zero. \mathbf{j}_{dis} is usually much smaller than the \mathbf{j}_{rf} , e.g. by a factor of 10^8 for Cu at

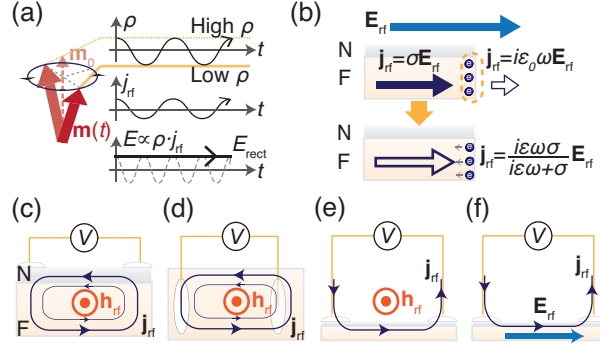


Fig. 6: (Color online) (a) Schematic illustration of mechanism of the rectification effect. (b) Induced rf current in an isolated conductor under an rf electric field, E_{rf} . ϵ_0 denotes the permittivity of a vacuum (c,d) Possible origins of stray rf currents: induced by in-plane (c) and out-of-plane (d) rf fields. (e,f) Rf currents picked up by the wires for the electric measurements.

$\omega/2\pi = 10$ GHz, and the phase of \mathbf{j}_{dis} is 90° different from the \mathbf{j}_{rf} , which indicates other consideration is necessary to explain previous results.

The Faraday's law causes an rf current from a microwave magnetic field. An in-plane microwave magnetic field induces an eddy current in the cross section of the bilayer systems [See Fig. 6(c)]. Though the current directions are opposite in the F and N layers, the microwave current can induce a non-zero rectification signal due to the difference between $\tilde{\rho}^F(\mathbf{m})$ and $\tilde{\rho}^N(\mathbf{m})$. This is one of plausible contributions to the experiments. For out-of-plane microwave field, the voltage appears only when the electrodes are placed off center from the rf-eddy-current distribution [See Fig. 6(d)]. Such an effect was studied in Ref. 86, which remarks that this effect can be eliminated by making the sample structure symmetric.

Consideration on wires connected to samples for the ISHE measurements leads to two additional contributions by the Ohm's law and Faraday's law, which are shown in Fig. 6(e,f). In one case, \mathbf{j}_{rf} can be proportional to $\sigma\mathbf{E}_{rf}$ with a factor considering the modification of the field due to a conducting sample. \mathbf{j}_{rf} is generated and is transmitted through the paired or twisted wires forming an microwave transmission line. In the other case, \mathbf{j}_{rf} is generated by the induction around a sample forming a pick-up coil with wires. In both the cases, rf currents only appear along the electrode direction.

As we discussed above, there are several mechanisms for the stray rf-current generation in cavities. The suppression of the rf current is not straightforward and thus the analysis based on \mathbf{j}_{rf} by leaving its magnitude, direction and phase undefined parameters, which are to be fitted with experimental data, is appropriate. The consideration of in-plane rf currents is enough for the analysis because the aforementioned mechanisms do not induce an rf current along the z direction unless a pathway for the rf current is formed in the z direction. This also holds for rf currents originating from the magnonic charge pumping,[87, 88] the ac ISHE current due to the ac SP,[89, 90] and other generation effects.

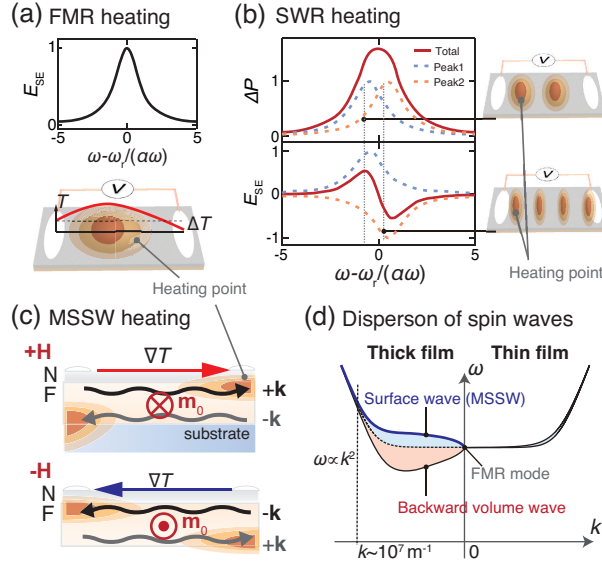


Fig. 7: (Color online) (a,b) Spectral shape of electromotive forces due to heat induced by the FMR (a) and SWR (b). (c) Induced ∇T due to MSSWs. When the magnetization is reversed, ∇T can change its sign, resulting in the same symmetry as the ISHE ($\mathbf{E}_{\text{ISHE}} \propto \mathbf{z} \times \mathbf{m}_0$). (d) Schematic illustration of difference in the dispersion relation for thin and thick ferromagnetic films.

2.5 Voltage generated by heating

Damping processes of magnetization dynamics generate heat, which can result in an electromotive force via thermoelectric effects. Thermoelectric effects, such as the Seebeck and Nernst effects, are seen in conducting materials by themselves regardless of the presence of the F layer. When a magnetization emits the absorbed power ΔP to phonons, a temperature gradient, $\nabla T \propto \Delta P \propto \text{Lor}(\omega, \omega_r)$, can be induced. ∇T is then formed into an electromotive force, e.g. $E_{\text{SE}} \propto \nabla T$ via the Seebeck effect. While the spectral shape of E_{SE} on the FMR is Lorentzian, it becomes complicated on the SWR in thick ferromagnetic films, which is also used to drive the SP.[91] The SWR gives a different heat profile on each resonance,[92] so that the sign of ∇T easily changes. When the neighboring peaks have different signs, the signal should look like the asymmetric Lorentzian, as shown in Fig. 7(b). As a result, the total thermoelectric voltage becomes the superposition of the symmetric and asymmetric Lorentzian for the SWR case.

The Seebeck effect contributes to the voltage signal when the heat profile produced by the FMR or SWR is not symmetrically distributed with respect to the electrodes for the voltage detection. In most systems, it does not have explicit dependence on the magnetization direction. However, there can be a case where ∇T is sensitive to the magnetization direction as is seen in a system comprised of a thick ferromagnetic film.[93]

In such films, spin waves known as magnetostatic surface spin waves (MSSWs) localize on the top and bottom surfaces of the F layer and propagate non-reciprocally.[94] MSSWs are demonstrated to convey heat to an arbitrary direction controlled by the magnetization polarization utilizing the non-reciprocity by unbalanced excitation of spin waves with wavevectors $+\mathbf{k}$ and $-\mathbf{k}$. [93] This results in $\nabla T \propto \mathbf{k}$ and thus induces a Seebeck voltage in the N layer, $\mathbf{E}_{\text{SE(MSSW)}} \propto \Delta P \mathbf{k}$. In microstrip antenna excitation, \mathbf{k} of the dominant MSSWs is reversed under the magnetization reversal, $\mathbf{m}_0 \rightarrow -\mathbf{m}_0$. [93, 95] This is because \mathbf{k} of the MSSWs localized at a surface with its normal \mathbf{n} is determined by $\mathbf{m}_0 \times \mathbf{n}$. [94] Consequently, the sign of the induced heat current by the MSSW is reversed, resulting in a thermoelectric signal with the same symmetry as the ISHE, i.e.

$$\mathbf{E}_{\text{SE(MSSW)}} = A_{\text{SE(MSSW)}} \Delta P \mathbf{z} \times \mathbf{m}_0, \quad (29)$$

where $A_{\text{SE(MSSW)}}$ is a constant determined by the Seebeck coefficient and the temperature profile due to the MSSW. In the cavity experiments on the SWR, though the spin waves with $+\mathbf{k}$ and $-\mathbf{k}$ are equally excited, asymmetries between the surfaces that these two modes are localized on can give the thermoelectric voltage in the same form as Eq. (29); as we place a N layer on top of the F layer, the inversion symmetry between the top and bottom layers is broken, so that the contributions from $+\mathbf{k}$ and $-\mathbf{k}$ give unequal contributions to ∇T in the N layer, which results in $\nabla T \propto \mathbf{k}$. Moreover, the existence of the substrate at the bottom surface may promote the asymmetry of the thermal conduction, possibly growing ∇T [See Fig. 7(c)]. Thus, the MSSW heating effect can appear regardless of the excitation methods in the F/N bilayer systems. This effect can be significant in materials with high thermoelectric conversion efficiency, such as low carrier density conductors.

Other contributions come from the transverse thermoelectric effects reflecting field or magnetization direction, such as the Nernst-Ettingshausen, anomalous Nernst effect (ANE) and spin Seebeck effect (SSE). Neglecting the angular difference between an applied field and \mathbf{m}_0 , the induced voltage is proportional to $\mathbf{m}_0 \times \nabla T$. Thus when ∇T is formed in the thickness direction, it gives an in-plane electromotive force

$$\mathbf{E}_{\text{TTE}} = A_{\text{TTE}} \Delta P \mathbf{z} \times \mathbf{m}_0, \quad (30)$$

where A_{TTE} denotes a proportionality constant determined by the magnitude of the transverse thermoelectric effects and ∇T along z direction. Importantly, \mathbf{E}_{TTE} shows the same symmetry as \mathbf{E}_{ISHE} .

3 Separation methods of SP-induced ISHE signal

In this section, we will introduce a guideline to select proper materials for the F layer and four methods to extract the spin current contribution from observed signals. Here, we discuss the microwave contribution to the voltage signals in terms of spectral shape, thickness, magnetization angle, and excitation frequency dependences. Understanding these dependences, the rectification effects can be isolated by a measurement of magnetization angular dependence, and the heating effects can be isolated by that of frequency dependence.

3.1 Suitable sample design for measurements of ISHE driven by SP

For electric measurements of the SP, an appropriate choice of materials for reducing the rectification and heating effects can improve the performance of the experiments. The first step of experiments of the ISHE induced by the SP thus is to consider the right choice of materials for the spin injector.

The rectification effects can be suppressed by using a material with low galvanomagnetic coefficients. The coefficients represented by $\Delta\rho_{AMR}$, ρ_{AHE}^F , $\Delta\rho_{SMR}$, and ρ_{AHE}^N in Eq. (23) are proportional to the signals. For the metallic spin injector, $Ni_{81}Fe_{19}$, so called Permalloy, is often used but other materials such as CoFe alloys with the low AMR ratio is a good candidate for the SP.[96, 97] Similarly, the SMR is known to be small compared to the AMR, and thus the use of a ferrimagnetic insulator is effective.[50]

The FMR and MSSW heating effects due to the conventional Seebeck effect can be minimized by making the sample structure symmetric about the electrodes and by reducing the thickness of the ferromagnetic layer d_F , respectively. The feature due to magnetostatic interaction is dominant around $|\mathbf{k}|d_F \sim 1$. [94] When d_F is decreased, such a value of \mathbf{k} increases and eventually reaches the exchange regime where the magnetostatic feature is lost. Figure 7 illustrates the dispersion relation of spin waves for thick and thin ferromagnetic films. The manifold of the dispersion shrinks as the film thickness reduces. The group velocity of the MSSWs correspondingly becomes smaller,[98] and the heat conveyer effect eventually disappears. Depending on the strength of the Seebeck effect, the appropriate thickness is below 100 nm for the measurements free from the MSSWs heating, which can be fabricated by pulsed laser deposition,[99] sputtering,[100] or metal-organic decomposition.[101] The MSSW contribution can also be confirmed by a control experiment with the insertion of a thin nonmagnetic insulator layer between the N and F layers because the nonmagnetic insulator cuts the spin transport but allows heat transport.[102]

3.2 Spectral shape dependence

First, let us introduce a way to separate a measured electric signal into symmetric and antisymmetric parts with respect to reversal of magnetization. We will explain why this simple method does not work for isolating the microwave effects. In addition to the spectral shape separation introduced here, measurements on the other dependences are strongly recommended.

As it is derived in Eqs. (21) and (25), the dc electromotive force on the FMR $\mathbf{E}_{tot} = \mathbf{E}_{ISHE} + \mathbf{E}_{rect} + \mathbf{E}_{SE(MSSW)} + \mathbf{E}_{TTE}$ has the two distinct parts proportional to $Lor(\omega, \omega_r)$ and $Asym(\omega, \omega_r)$. By fitting an observed signal by

$$\mathbf{E}_{tot} = \mathbf{E}_{sym}Lor(\omega, \omega_r) + \mathbf{E}_{asym}Asym(\omega, \omega_r), \quad (31)$$

the separation can be done, where $E_{sym(asym)}$ is the magnitude of the $Lor(\omega, \omega_r)$ ($Asym(\omega, \omega_r)$) part (See Fig. 8). The earlier naive discussions attribute the whole E_{sym} due to the ISHE, but this assumption does not hold as is discussed below. Generally,

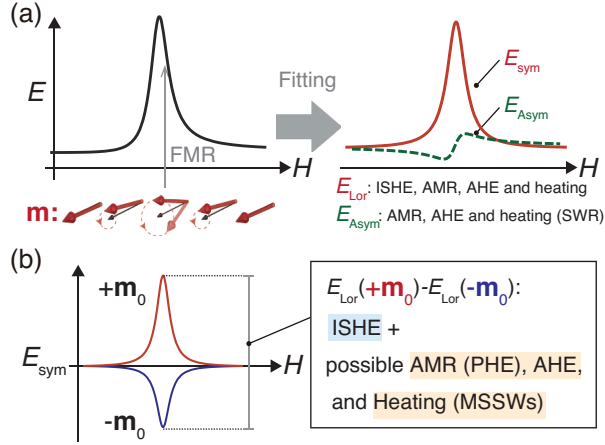


Fig. 8: (Color online) (a) Common procedure for extracting the ISHE contribution. (b) The origins which can show the sign change under the magnetization reversal. Lorentzian part with the sign change is not only due to the ISHE, but also due to the microwave extrinsic effects.

E_{sym} includes not only the ISHE component but also the rectification contribution.[32, 49] For example, in a TE_{011} cavity with the rf field h_{rf} in the y direction and an rf current along the x direction with $j_{\text{rf}} \propto ih_{\text{rf}}$, the y -component of Eq. (26) leads to

$$E_{\text{sym,ISHE}}^y \propto \frac{\omega_\phi}{(\omega_\theta + \omega_\phi)^2} \sin \theta_M,$$

$$E_{\text{sym,rect}}^y \propto \frac{(\rho_{\text{AHE}} \omega_{\theta\phi} - \Delta \rho_{\text{AMR}} \omega_\phi)}{\omega(\omega_\theta + \omega_\phi)} \sin \theta_M \quad (32)$$

at $\phi_M = 0$. [32] The configuration is depicted in Fig. 4(b). E_{sym} includes signals due to the rectification effects and, importantly, possesses the same symmetry as the ISHE signal, i.e. $\sin \theta_M$. Therefore, the part of the Lorentzian signal with the sign change following to the magnetization reversal cannot be attributed to only the ISHE without further examinations. In Ref. 32, a separation of the contributions based on the difference in the pre-factors, i.e. $\omega_{\theta\phi}$, ω_ϕ , ω , during the θ_M scan is suggested and will be introduced in Sect. 3.4. Note that Eq. (32) holds only when the rf current is constant during the scan. However, the stray rf current often shows angular dependence.[103]

The heating effect due to transverse thermoelectric effects can also induce the similar signal to the ISHE, which is given by

$$E_{\text{sym,TTE}}^y \propto \frac{\omega_\phi}{\omega_\theta + \omega_\phi} \sin \theta_M. \quad (33)$$

The FMR heating contribution discussed in Sect. 2.5 can be extracted by the frequency dependence measurement. The MSSW heating contribution discussed in Sect. 2.5 is

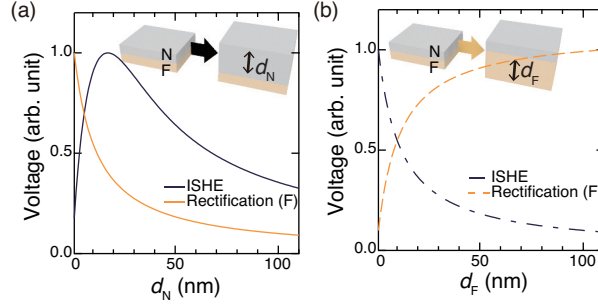


Fig. 9: (Color online) (a,b) Thickness d_N (a) and d_F (b) dependence of the ISHE and rectification signals. We assume $\lambda = 10$ nm and normalize the curves by the maximum value in the plot regime.

unable to be removed until the F layer thickness is reduced. One possible solution for handling this difficulty is finding this contribution from the calculation based on the Seebeck coefficient following a temperature profile measurement as is done in Ref. 104.

An asymmetric component is a sign of contribution from the rectification effects although the reverse is not true because rectification signals can have only the Lorentzian component. If one knows the direction of the rf current, then the asymmetric component might be a good measure to determine its magnitude and thus the rectification contribution. The direction may be estimated by measuring the voltage along other directions as shown in Ref. 103, 105.

3.3 Thickness dependence

The voltage signals from the ISHE and rectification effects have different dependence on the thickness of the F and N layers.[77] For a bilayer where the galvanomagnetic effects in the F layer is dominant, the symmetric Lorentzian signal after taking the difference between \mathbf{m}_0 and $-\mathbf{m}_0$ is expressed in the following form,

$$E_{\text{sym,ISHE}}^y = \frac{E_{\text{ISHE}}^0}{\sigma_N d_N + \sigma_F d_F} \tanh \frac{d_N}{2\lambda}, \quad (34)$$

$$E_{\text{sym,rect}}^y = \frac{d_F E_{\text{rect}}^0}{\sigma_N d_N + \sigma_F d_F}, \quad (35)$$

where E_{ISHE}^0 and E_{rect}^0 are respectively determined by Eqs. (21) and (26). Regarding E_{ISHE}^0 (or $\langle j_s^{F/N} \rangle_t$) and E_{rect}^0 as constants, the d_N dependence of Eq. (34) reads a tangent hyperbolic function divided by the total resistance, which shows a positive peak around $d_N \approx 2\lambda$ [See Fig. 9(a)]. The d_N dependence of the rectification contribution shows monotonic decrease as d_N increases. The distinction between these two becomes difficult for $d_N > \lambda_N$, because both show just decrease as d_N increases [See Fig. 9(b)]. On the other hand, the d_F dependence shows clear difference; as d_F increases, the ISHE

and rectification contributions respectively show monotonic decrease and increase before saturation. This is because the SP (the rectification effects) induced voltage is electrically-shorted by the additional F (N) layer. This contrary dependence of the SP and rectification contributions is very useful to separate them. For a practice analysis, thickness dependence of parameters should be considered, such as $g_{\text{eff},r}^{\uparrow\downarrow}$, $\tilde{\rho}^F$, and $j_{\text{rf}}(z)$.

The FMR and MSSW heating effects can complicate the thickness dependence of the signal because the induced temperature gradient depends on sample structure and environment. Therefore, it is highly recommended to carefully consider an appropriate design of the samples as described in Sect. 3.1.

3.4 Angular dependence

The magnetization angular dependence of \mathbf{E}_{ISHE} is derived in Ref. 106 and that of \mathbf{E}_{rect} due to the AMR (PHE), AHE and SMR can be found in Refs. 32, 50, 56, 107, 108. Here, we will focus on the ISHE and rectification effects, because the heating effects can not be isolated by the angular dependence. The angular dependence can be studied by two types of rotation: out-of-plane angular dependence (OP) and in-plane angular dependence (IP), which are shown in Figs. 10 and 11. In addition, there are two different means to excite the ferromagnet: applying an rf excitation field in OP or IP. Here, these four configurations are considered in a film system with uniaxial anisotropy perpendicular to the film plane, which is relevant to most of experiments. Such systems are described by the magnetostatic energy:

$$F_m = -\mathbf{m} \cdot \mathbf{H}_0 + \frac{I_s^2}{2\mu_0} m_z^2 - K_u m_z^2, \quad (36)$$

where \mathbf{H}_0 is an applied external field, given by $\mathbf{H}_0 = H_0 (\sin \theta_H \cos \phi_H \mathbf{e}_x + \sin \theta_H \sin \phi_H \mathbf{e}_y + \cos \theta_H \mathbf{e}_z)$, and K_u denotes the perpendicular anisotropy constant. Equation (36) reduces Eq. (12) to

$$\omega_\theta = \gamma [\mu_0 H_0 \cos(\theta_H - \theta_M) - I_{\text{eff}} \cos^2 \theta_M], \quad (37)$$

$$\omega_\phi = \gamma [\mu_0 H_0 \cos(\theta_H - \theta_M) - I_{\text{eff}} \cos(2\theta_M)], \quad (38)$$

and $\omega_{\theta\phi} = 0$, where I_{eff} denotes the effective magnetization $I_{\text{eff}} = I_s - 2\mu_0 K_u / I_s$, and θ_H (ϕ_H) denotes the polar (azimuthal) angle in the spherical coordinate as shown in Fig. 10(a). The resonance field H_r is determined by H_0 which simultaneously satisfies $\omega_r = \sqrt{\omega_\theta \omega_\phi}$ and $\mathbf{m}_0 \times \mathbf{H}_{\text{eff}} = 0$, which is reduced to

$$2\mu_0 H_0 \sin(\theta_H - \theta_M) + I_{\text{eff}} \sin(2\theta_M) = 0 \quad (39)$$

and $\phi_H = \phi_M$. Note that in the following calculation we still use $\omega_{\theta(\phi)}$ for simple notation but impose $\omega_{\theta\phi} = 0$.

In the setup for the OP angular dependence measurements, the magnetization is rotated in the xz plane ($\phi_M = 0$) and electrodes for detecting the ISHE voltage are placed in the y axis [See Fig. 10(a)]. An IP excitation field, h_{rf} along the y axis, induces

$$E_{\text{sym,ISHE}}^y = A_{\text{ISHE}} \frac{\omega_\phi}{(\omega_\theta + \omega_\phi)^2} \sin \theta_M, \quad (40)$$

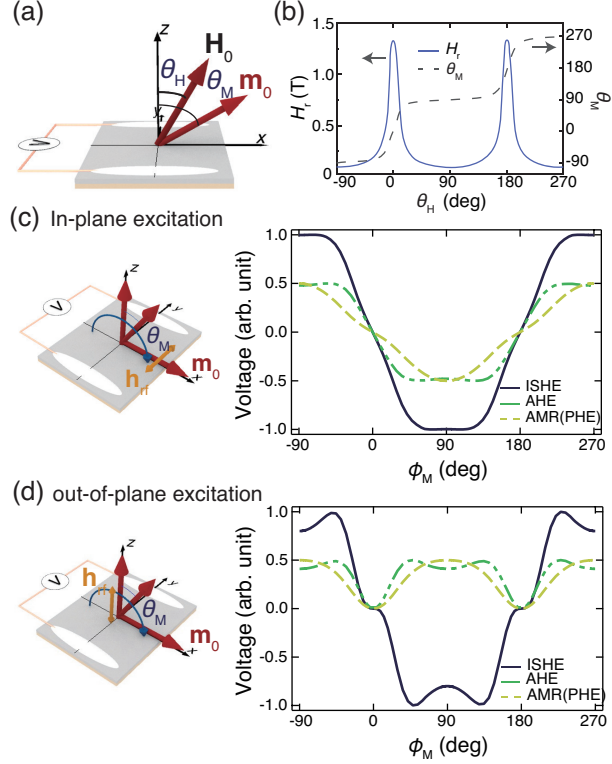


Fig. 10: (Color online) (a) Schematic illustration of out-of-plane (OP) angular dependence measurement, where \mathbf{m}_0 and \mathbf{H}_0 points different direction due to the demagnetizing and uniaxial anisotropy fields. (b) H_t and θ_M as a function of θ_H . (c,d) angular dependence of the ISHE and rectification signals for the in-plane excitation (c) and OP excitation (d). The ISHE and rectification signals are normalized to be 1 and 0.5, respectively.

$$E_{\text{sym,rect}}^y = A_{\text{rect}} \frac{(\omega \rho_{\text{AHE}} \text{Re}[j_{\text{rf}}^{x*}] + \omega_\phi \Delta \rho_{\text{AMR}} \text{Im}[j_{\text{rf}}^{x*}])}{\omega(\omega_\theta + \omega_\phi)} \sin \theta_M, \quad (41)$$

where the coefficients A are given by

$$A_{\text{ISHE}} = w \tilde{R}_{\text{tot}} \theta_{\text{SHE}} \frac{2e}{\hbar} \lambda \tanh \frac{d_N}{2\lambda} \frac{\hbar g_{r,\text{eff}}^{\uparrow\downarrow}}{4\pi} \frac{\gamma^2 \mu_0^2 h_{\text{rf}}^2}{\alpha^2}, \quad (42)$$

$$A_{\text{rect}} = \tilde{R}_{\text{tot}} \frac{\sigma_{\text{F}} d_{\text{F}}}{2} \frac{\gamma \mu_0 h_{\text{rf}}}{\alpha}, \quad (43)$$

both of which are proportional to $\sin \theta_M$. In Ref. 32, the separation is done based on the difference in the dependence on ω_θ (θ_M) and ω_ϕ (θ_M) between the ISHE and rectification voltages, which is because they have different responses to the effective

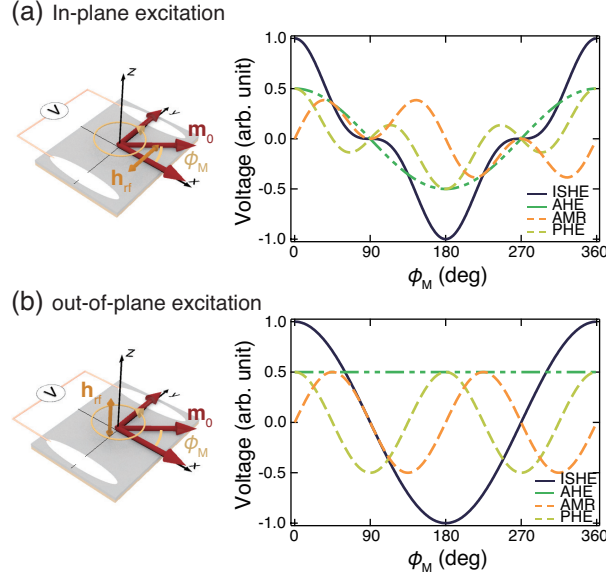


Fig. 11: (Color online) (a, b) In-plane (IP) angular dependence of the ISHE and rectification signals for the IP excitation (a) and out-of-plane excitation (b). The ISHE and rectification signals are normalized to be 1 and 0.5, respectively. PHE denotes the AMR signal caused by j_{rf}^x .

field sweeping over θ_H . Figure 10(b) shows H_r and θ_M as a function of θ_H calculated with $\gamma = 1.79 \times 10^{11} \text{ T}^{-1} \text{ s}^{-1}$ and $I_{\text{eff}} = 1 \text{ T}$. Figure 10(c) shows the θ_M dependence of E_{ISHE} and E_{rect} , which possess similar form, but slight difference seen in the solid and dashed curves. This similarity can be a large source of error in data fitting.

An OP excitation field, h_z , induces

$$E_{\text{sym,ISHE}}^y = A_{\text{ISHE}} \frac{\omega_\theta}{(\omega_\theta + \omega_\phi)^2} \sin^3 \theta_M, \quad (44)$$

$$E_{\text{sym,rect}}^y = A_{\text{rect}} \frac{(\omega \Delta \rho_{\text{AMR}} \text{Re}[j_{rf}^{x*}] - \omega_\theta \rho_{\text{AHE}} \text{Im}[j_{rf}^{x*}])}{\omega (\omega_\theta + \omega_\phi)} \sin^2 \theta_M, \quad (45)$$

[See Fig. 10(d)]. At a glance, the difference in the two signals are clear, namely $E_{\text{rect}}^y \propto \sin^2 \theta_M$ and $E_{\text{ISHE}}^y \propto \sin^3 \theta_M$. However, when $j_{rf} \propto \sin \theta_M$ holds, the contributions cannot be separated by the harmonic functions.

Similarly to the OP angular dependence in the OP excitation, the IP angular dependence excited by an IP rf field has the same difficulty. In the setup, the magnetization is rotated in the xy plane ($\theta_M = 90^\circ$) and electrodes for detecting the ISHE voltage are placed in the y axis. The electromotive forces in the y direction are

$$E_{\text{sym,ISHE}}^y = A_{\text{ISHE}} \frac{\omega_\phi}{\omega (\omega_\theta + \omega_\phi)^2} \cos^3 \phi_M, \quad (46)$$

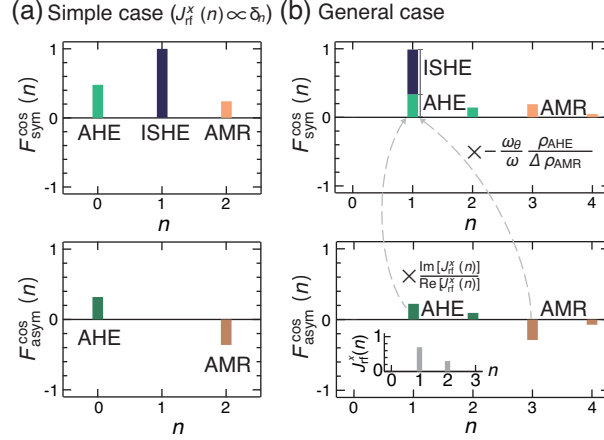


Fig. 12: (Color online) (a,b) Analysis scheme based on the Fourier cosine coefficients: case for the constant rf current (a) and case for angular dependent rf current (b) during the magnetization angle scan in the film plane. The inset shows the magnitude of the Fourier cosine coefficient of the complex j_{rf}^x .

$$E_{\text{sym,rect}}^y = A_{\text{rect}} \cos \phi_M \frac{\omega_\phi \Delta \rho_{\text{AMR}} \left(\cos(2\phi_M) \text{Im} [j_{\text{rf}}^{x*}] + \sin(2\phi_M) \text{Im} [j_{\text{rf}}^{y*}] \right) + \omega \rho_{\text{AHE}} \text{Re} [j_{\text{rf}}^{x*}]}{\omega (\omega_\theta + \omega_\phi)} \quad (47)$$

[See Fig. 11(a)]. In this configuration, the ISHE and AMR contributions mix even for the simplest condition that the rf current is angular-independent.

The IP angular dependence excited by an OP rf field has an advantage to the previous three angular dependences because the AMR and AHE show different symmetric angular dependences in the IP configuration. An OP excitation field, h_z , induces

$$E_{\text{sym,ISHE}}^y = A_{\text{ISHE}} \frac{\omega_\theta}{(\omega_\theta + \omega_\phi)^2} \cos \phi_M, \quad (48)$$

$$E_{\text{sym,rect}}^y = A_{\text{rect}} \frac{\omega \Delta \rho_{\text{AMR}} \left(\cos(2\phi_M) \text{Re} [j_{\text{rf}}^{x*}] + \sin(2\phi_M) \text{Re} [j_{\text{rf}}^{y*}] \right) - \omega_\theta \rho_{\text{AHE}} \text{Im} [j_{\text{rf}}^{x*}]}{\omega (\omega_\theta + \omega_\phi)}. \quad (49)$$

For the simplest case where $j_{x(y)}^{\text{rf}}$ is constant during the rotation, importantly, the ISHE, AMR and AHE show the different angular dependences, $\cos \phi_M$, $\cos(2\phi_M)$, and constant [Fig. 11(b)]. Thus, fitting the result using the harmonic functions gives the ISHE contribution directly. Figure 11 shows the calculation result based on Eqs. (48) and (49).

When $j_{x(y)}^{\text{rf}}$ has an angular dependence, an analysis method based on the Fourier series coefficient is effective in the measurements on the IP angular dependence with

OP excitation. The n -th Fourier cosine coefficient of the voltage is given by

$$F_{\text{sym}}^{\text{cos}}(n) = \frac{\omega_{\theta} A_{\text{ISHE}}}{(\omega_{\theta} + \omega_{\phi})^2} \delta_{n-1} + \frac{A_{\text{rect}}}{\omega(\omega_{\theta} + \omega_{\phi})} \left(\omega \Delta \rho_{\text{AMR}} \text{Re} \left[J_{\text{rf}}^x(n-2) \right] - \omega_{\theta} \rho_{\text{AHE}} \text{Im} \left[J_{\text{rf}}^x(n) \right] \right), \quad (50)$$

$$F_{\text{asym}}^{\text{cos}}(n) = \frac{A_{\text{rect}}}{\omega(\omega_{\theta} + \omega_{\phi})} \left(-\omega \Delta \rho_{\text{AMR}} \text{Im} \left[J_{\text{rf}}^x(n-2) \right] - \omega_{\theta} \rho_{\text{AHE}} \text{Re} \left[J_{\text{rf}}^x(n) \right] \right), \quad (51)$$

where δ_n denotes the Kronecker delta function and $J_{\text{rf}}^x(n)$ is the n -th Fourier cosine coefficient of j_{rf}^x . Figure 12(a) shows an expected intensity of the coefficients for $J_{\text{rf}}^x(n) \propto \delta_n$. The contributions are clearly separated. Figure 12(b) shows a calculation of the coefficients for $J_{\text{rf}}^x(n)$ with $J_{\text{rf}}^x(1) \neq 0$. $J_{\text{rf}}^x(1)$ can induces an ISHE-like signal via the AHE. However, this contribution can be removed by comparing symmetric and antisymmetric components because there is a relation,

$$F_{\text{sym}}^{\text{cos}}(1) = -\frac{\omega_{\theta}}{\omega} \frac{\rho_{\text{AHE}}}{\Delta \rho_{\text{AMR}}} F_{\text{asym}}^{\text{cos}}(3),$$

in the absence of the ISHE. Therefore, the factor above gives the upper limit of the Lorentzian part due to the AHE. When $\omega_{\theta}(\omega_{\phi})$ possesses ϕ_M dependence because of a magnetic anisotropy field in-plane, Eq. (51) should be recalculated by considering the Fourier coefficients of ω_{θ} and ω_{ϕ} . Note that when $\Delta \rho = 0$ but $\rho_{\text{AHE}} \neq 0$, this method can not be applied, and it is better to change a material for the F layer or to try a measurement on the ferromagnetic layer thickness dependence described in Sect. 3.3.

3.5 Frequency dependence

Here, we focus on the difference in the frequency dependence of the signals from the ISHE and the microwave effects. The frequency dependence has attracted much attention for its nonlinear physics coming from magnon-magnon interactions.[109–113] Our interest is the linear excitation regime in which the derived equations for the FMR can be used.[114] The heating effects show a clear difference from the ISHE and rectification effects, so that this method works effectively for removing the heating contribution.

In the calculation we consider a system with field along the x and rf field along the y axis, i.e. the IP excitation at $\theta_M = 90^\circ$ and $\phi_M = 0^\circ$. This configuration is often used in measurements with a microstrip line or a coplanar waveguide. The frequency dependence of the ISHE and rectification signals are respectively given by

$$E_{\text{sym,ISHE}}^y = A_{\text{ISHE}} \frac{\omega_{\phi}}{(\omega_{\theta} + \omega_{\phi})^2} \quad (52)$$

and

$$E_{\text{sym,rect}}^y = A_{\text{rect}} \frac{\left(\omega \rho_{\text{AHE}} \text{Re} \left[j_{\text{rf}}^{x*} \right] + \omega_{\phi} \Delta \rho_{\text{AMR}} \text{Im} \left[j_{\text{rf}}^{x*} \right] \right)}{\omega(\omega_{\theta} + \omega_{\phi})}. \quad (53)$$

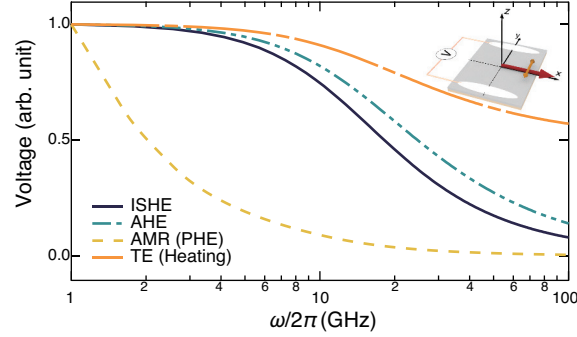


Fig. 13: (Color online) Frequency dependence of signals induced by the ISHE, rectification, and heating effects. The curves are normalized at $\omega/2\pi = 1$ GHz. Other parameters are same as those used for the OP angular dependence calculation.

The electromotive force due to the heating, proportional to microwave absorption ΔP , is given by

$$E_{\text{sym,TE}}^y = A_{\text{TE}} \frac{\omega_\phi}{(\omega_\theta + \omega_\phi)} \quad (54)$$

with $A_{\text{TE}} = \frac{\gamma\mu_0 h_{\text{eff}}^2}{2\alpha} (A_{\text{TTE}} + A_{\text{SE(MSSW)}})$. Figure 13 shows the calculated frequency dependence of the ISHE, rectification effects, and heating effects. Since the ISHE and AHE are similar, the separation between the ISHE and rectification signals based on the frequency will not be so accurate. The difference between the SP and the rectification effects comes from the ellipticity of magnetization precession due to demagnetizing and anisotropic fields. At frequencies $\omega > \gamma I_{\text{eff}}$, the large external field necessary for the FMR makes the precession trajectory circular, so that both of them become proportional to $1/\omega$. The heating is proportional to ΔP [Eq. (16)] and is proportional to $\omega_{\theta(\phi)}/\omega$, which reaches constant at high frequencies. This feature is distinct from the others. The studies on the frequency dependence [109–112, 114] indicates that the thermoelectric contribution in the ferrimagnetic insulator/Pt bilayer systems is not dominant for the microwave spin pumping experiments.

4 Summary

In this article, we reviewed voltage generation by the SP-induced ISHE, the rectification effects due to galvanomagnetic effects, and the heating effects due to thermoelectric effects. The electric detection of a spin current induced by the SP using the ISHE is a strong method to study spin physics in a material of interest. The key for the study is clear separation between the ISHE and the other extrinsic contributions. In some configurations, they look similar to each other, but by employing the separation methods introduced here, one can perform a reliable measurement with high accuracy. Figure 14 summarizes the recommended method by which the accuracy can be easily

Material of F Layer	Method	Spectral Shape	Thickness	Magnetization Angle	Excitation Frequency
	Origin				
Thin Metal	Rectification	×	✓ (d_F) Δ (d_N)	✓ (IP) Δ (OP)	Δ
	Heating	Δ	—	Δ (IP) Δ (OP)	✓
Thin Insulator	Rectification	Δ	— (d_F) Δ (d_N)	✓ (IP) Δ (OP)	Δ
	Heating	Δ	—	Δ (IP) Δ (OP)	✓
Thick Insulator	Rectification	Δ	— (d_F) Δ (d_N)	✓ (IP) Δ (OP)	Δ
	Heating	×	—	× (IP) × (OP)	✓

Fig. 14: (Color online) Summary of methods for measuring the SP-induced ISHE. It is written which effect can be separated (✓) or cannot be separated (×) by using combination of the corresponding material for the spin injector (F) layer and the measurement. — denotes the non applicable separation method. Δ denotes the moderate separation method when galvanomagnetic or transverse thermoelectric effects are not negligibly small. Here, we assume that the MSSW heating is dominant among the heating-induced signals. The use of a thin ferrimagnetic insulator is the best way to explore spin physics by using the spin pumping, because the magnitude of the galvanomagnetic effects and MSSW heating is expected to be small compared to that in metallic and thick ferromagnets.

obtained. For a better experiment, a material of interest should be on top of a thin ferrimagnetic insulator film, which reduces both the rectification and heating effects. For systems with metallic ferromagnet, the IP magnetization angular dependence is the best configuration to clarify the differences among the voltage signals of the ISHE and the rectification effects, because the ISHE is sensitive to spin polarization while the AMR is sensitive to the magnitude than the polarization. The separation schemes discussed in this article provides a better way to extract the SP-originated signals. We thus anticipate that the experimental schemes help further material investigations and contribute to the development of novel spintronic devices.

Acknowledgment

The authors thank K. Sato, K. Uchida, and D. Hirobe for valuable discussions and suggestions. This work was supported by Grant-in-Aid for Scientific Research on Innovative Area, “Nano Spin Conversion Science” (No. 26103002, 26103005) from MEXT, Japan, and E-IMR, Tohoku University.

References

- [1] J. A. Katine, F. J. Albert, R. A. Buhrman, E. B. Myers, and D. C. Ralph: *Physical Review Letters* **84** (2000) 3149.
- [2] V. E. Demidov, S. Urazhdin, E. Edwards, M. Stiles, R. McMichael, and S. Demokritov: *Physical Review Letters* **107** (2011) 107204.
- [3] L. Berger: *Physical Review B* **54** (1996) 9353.
- [4] D. Ralph and M. D. Stiles: *Journal of Magnetism and Magnetic Materials* **320** (2008) 1190.
- [5] Y. Kajiwara, K. Harii, S. Takahashi, J. Ohe, K. Uchida, M. Mizuguchi, H. Umezawa, H. Kawai, K. Ando, K. Takanashi, et al.: *Nature* **464** (2010) 262.
- [6] L. Cornelissen, J. Liu, R. Duine, J. B. Youssef, and B. Van Wees: *Nature Physics* **11** (2015) 1022.
- [7] S. T. B. Goennenwein, R. Schlitz, M. Pernpeintner, K. Ganzhorn, M. Althammer, R. Gross, and H. Huebl: *Applied Physics Letters* **107** (2015).
- [8] K. Uchida, S. Takahashi, K. Harii, J. Ieda, W. Koshibae, K. Ando, S. Maekawa, and E. Saitoh: *Nature* **455** (2008) 778.
- [9] K. Uchida, J. Xiao, H. Adachi, J.-i. Ohe, S. Takahashi, J. Ieda, T. Ota, Y. Kajiwara, H. Umezawa, H. Kawai, et al.: *Nature Materials* **9** (2010) 894.
- [10] C. Jaworski, J. Yang, S. Mack, D. Awschalom, J. Heremans, and R. Myers: *Nature Materials* **9** (2010) 898.
- [11] A. Kirihara, K.-i. Uchida, Y. Kajiwara, M. Ishida, Y. Nakamura, T. Manako, E. Saitoh, and S. Yorozu: *Nature Materials* **11** (2012) 686.
- [12] K. Uchida, H. Adachi, T. Kikkawa, A. Kirihara, M. Ishida, S. Yorozu, S. Maekawa, and E. Saitoh: *Proceedings of the IEEE PP* (2016) 1.
- [13] H. Nakayama, M. Althammer, Y.-T. Chen, K. Uchida, Y. Kajiwara, D. Kikuchi, T. Ohtani, S. Geprägs, M. Opel, S. Takahashi, et al.: *Physical Review Letters* **110** (2013) 206601.
- [14] Y.-T. Chen, S. Takahashi, H. Nakayama, M. Althammer, S. T. Goennenwein, E. Saitoh, and G. E. Bauer: *Physical Review B* **87** (2013) 144411.
- [15] M. Althammer, S. Meyer, H. Nakayama, M. Schreier, S. Altmannshofer, M. Weiler, H. Huebl, S. Geprägs, M. Opel, R. Gross, et al.: *Physical Review B* **87** (2013) 224401.
- [16] E. Saitoh, M. Ueda, H. Miyajima, and G. Tatara: *Applied Physics Letters* **88** (2006) 182509.

-
- [17] T. Kimura, Y. Otani, T. Sato, S. Takahashi, and S. Maekawa: *Physical Review Letters* **98** (2007) 156601.
- [18] B. Miao, S. Huang, D. Qu, and C. Chien: *Physical Review Letters* **111** (2013) 066602.
- [19] L. Liu, C.-F. Pai, Y. Li, H. Tseng, D. Ralph, and R. Buhrman: *Science* **336** (2012) 555.
- [20] O. Mosendz, J. Pearson, F. Fradin, G. Bauer, S. Bader, and A. Hoffmann: *Physical Review Letters* **104** (2010) 046601.
- [21] H. Wang, C. Du, Y. Pu, R. Adur, P. C. Hammel, and F. Yang: *Physical Review Letters* **112** (2014) 197201.
- [22] S. O. Valenzuela and M. Tinkham: *Nature* **442** (2006) 176.
- [23] J. Mendes, R. Cunha, O. A. Santos, P. Ribeiro, F. Machado, R. Rodríguez-Suárez, A. Azevedo, and S. Rezende: *Physical Review B* **89** (2014) 140406.
- [24] Y. Niimi and Y. Otani: *Reports on Progress in Physics* **78** (2015) 124501.
- [25] A. Azevedo, L. H. Vilela Leão, R. L. Rodríguez-Suarez, A. B. Oliveira, and S. M. Rezende: *Journal of Applied Physics* **97** (2005) 10C715.
- [26] J. Wunderlich, B. Kaestner, J. Sinova, and T. Jungwirth: *Physical Review Letters* **94** (2005) 047204.
- [27] J. Sinova, D. Culcer, Q. Niu, N. Sinitsyn, T. Jungwirth, and A. MacDonald: *Physical Review Letters* **92** (2004) 126603.
- [28] Y. Kato, R. Myers, A. Gossard, and D. Awschalom: *Science* **306** (2004) 1910.
- [29] K. Ando, S. Takahashi, J. Ieda, H. Kurebayashi, T. Trypiniotis, C. Barnes, S. Maekawa, and E. Saitoh: *Nature Materials* **10** (2011) 655.
- [30] K. Ando and E. Saitoh: *Nature Communications* **3** (2012) 629.
- [31] S. Murakami, N. Nagaosa, and S.-C. Zhang: *Science* **301** (2003) 1348.
- [32] L. Chen, F. Matsukura, and H. Ohno: *Nature Communications* **4** (2013) 2055.
- [33] D. Sun, K. J. van Schooten, M. Kavand, H. Malissa, C. Zhang, M. Groesbeck, C. Boehme, and Z. Valy Vardeny: *Nat Mater* **advance online publication** (2016).
- [34] K. Ando, S. Watanabe, S. Mooser, E. Saitoh, and H. Siringhaus: *Nature Materials* **12** (2013) 622.
- [35] S. Dushenko, M. Koike, Y. Ando, T. Shinjo, M. Myronov, and M. Shiraiishi: *Physical Review Letters* **114** (2015) 196602.

-
- [36] Y. Shiomi, K. Nomura, Y. Kajiwara, K. Eto, M. Novak, K. Segawa, Y. Ando, and E. Saitoh: *Physical Review Letters* **113** (2014) 196601.
- [37] Y. Ando, T. Hamasaki, T. Kurokawa, K. Ichiba, F. Yang, M. Novak, S. Sasaki, K. Segawa, Y. Ando, and M. Shiraishi: *Nano Letter* **14** (2014) 6226.
- [38] A. Mellnik, J. Lee, A. Richardella, J. Grab, P. Mintun, M. Fischer, A. Vaezi, A. Manchon, E.-A. Kim, N. Samarth, et al.: *Nature* **511** (2014) 449.
- [39] J. Hirsch: *Physical Review Letters* **83** (1999) 1834.
- [40] A. Hoffmann: *Magnetics, IEEE Transactions on* **49** (2013) 5172.
- [41] J. Sinova, S. O. Valenzuela, J. Wunderlich, C. H. Back, and T. Jungwirth: *Review of Modern Physics* **87** (2015) 1213.
- [42] S. Mizukami, Y. Ando, and T. Miyazaki: *Physical Review B* **66** (2002) 104413.
- [43] Y. Tserkovnyak, A. Brataas, G. E. W. Bauer, and B. I. Halperin: *Review of Modern Physics* **77** (2005) 1375.
- [44] Y. Tserkovnyak, A. Brataas, and G. E. Bauer: *Physical Review Letters* **88** (2002) 117601.
- [45] K. Ando, S. Takahashi, J. Ieda, Y. Kajiwara, H. Nakayama, T. Yoshino, K. Harii, Y. Fujikawa, M. Matsuo, S. Maekawa, et al.: *Journal of Applied Physics* **109** (2011) 103913.
- [46] E. Shikoh, K. Ando, K. Kubo, E. Saitoh, T. Shinjo, and M. Shiraishi: *Physical Review Letters* **110** (2013) 127201.
- [47] S. Watanabe, K. Ando, K. Kang, S. Mooser, Y. Vaynzof, H. Kurebayashi, E. Saitoh, and H. Sirringhaus: *Nature Physics* **10** (2014) 308.
- [48] H. Inoue, K. Harii, K. Ando, K. Sasage, and E. Saitoh: *Journal of Applied Physics* **102** (2007) 083915.
- [49] A. Azevedo, L. Vilela-Leão, R. Rodríguez-Suárez, A. L. Santos, and S. Rezende: *Physical Review B* **83** (2011) 144402.
- [50] R. Iguchi, K. Sato, D. Hirobe, S. Daimon, and E. Saitoh: *Applied Physics Express* **7** (2013) 013003.
- [51] L. Bai, P. Hyde, Y. S. Gui, C.-M. Hu, V. Vlaminck, J. E. Pearson, S. D. Bader, and A. Hoffmann: *Physical Review Letters* **111** (2013) 217602.
- [52] L. Chen, S. Ikeda, F. Matsukura, and H. Ohno: *Applied Physics Express* **7** (2013) 013002.
- [53] F. Bakker, J. Flipse, A. Slachter, D. Wagenaar, and B. van Wees: *Physical Review Letters* **108** (2012) 167602.

-
- [54] H. Schultheiss, J. E. Pearson, S. D. Bader, and A. Hoffmann: *Physical Review Letters* **109** (2012) 237204.
- [55] Z. Qiu, Y. Kajiwara, K. Ando, Y. Fujikawa, K.-i. Uchida, T. Tashiro, K. Harii, T. Yoshino, and E. Saitoh: *Applied Physics Letters* **100** (2012) 022402.
- [56] W. G. Egan and H. J. Juretschke: *Journal of Applied Physics* **34** (1963) 1477.
- [57] W. M. Moller and H. J. Juretschke: *Physical Review B* **2** (1970) 2651.
- [58] A. Yamaguchi, H. Miyajima, T. Ono, Y. Suzuki, S. Yuasa, A. Tulapurkar, and Y. Nakatani: *Applied Physics Letters* **90** (2007) 2507.
- [59] Y. Gui, N. Mecking, X. Zhou, G. Williams, and C. M. Hu: *Physical Review Letters* **98** (2007).
- [60] T. Chiba, G. E. Bauer, and S. Takahashi: *Physical Review Applied* **2** (2014) 034003.
- [61] L. Liu, T. Moriyama, D. Ralph, and R. Buhrman: *Physical Review Letters* **106** (2011) 036601.
- [62] T. L. Gilbert: *Magnetics, IEEE Transactions on* **40** (2004) 3443.
- [63] H. Jiao and G. E. Bauer: *Physical Review Letters* **110** (2013) 217602.
- [64] M. Weiler, M. Althammer, M. Schreier, J. Lotze, M. Pernpeintner, S. Meyer, H. Huebl, R. Gross, A. Kamra, J. Xiao, et al.: *Physical Review Letters* **111** (2013) 176601.
- [65] J.-C. Rojas-Sánchez, N. Reyren, P. Laczkowski, W. Savero, J.-P. Attané, C. Deranlot, M. Jamet, J.-M. George, L. Vila, and H. Jaffrès: *Physical Review Letters* **112** (2014) 106602.
- [66] W. Zhang, W. Han, X. Jiang, S.-H. Yang, and S. S. Parkin: *Nature Physics* **11** (2015) 496.
- [67] K. Xia, P. Kelly, G. E. Bauer, A. Brataas, and I. Turek: *Physical Review B* **65** (2002) 220401.
- [68] X. Jia, K. Liu, K. Xia, and G. E. W. Bauer: *Europhysics Letters* **96** (2011) 17005.
- [69] K. Ando, S. Takahashi, K. Harii, K. Sasage, J. Ieda, S. Maekawa, and E. Saitoh: *Physical Review Letters* **101** (2008) 036601.
- [70] Y. Tserkovnyak, A. Brataas, and G. E. Bauer: *Physical Review B* **66** (2002) 224403.
- [71] M. Johnson, P. Bloemen, F. Den Broeder, and J. De Vries: *Reports on Progress in Physics* **59** (1996) 1409.

-
- [72] K. Lenz, H. Wende, W. Kuch, K. Baberschke, K. Nagy, and A. Jánossy: *Physical Review B* **73** (2006) 144424.
- [73] K. Zakeri, J. Lindner, I. Barsukov, R. Meckenstock, M. Farle, U. Von Hörsten, H. Wende, W. Keune, J. Rucker, S. Kalarickal, et al.: *Physical Review B* **76** (2007) 104416.
- [74] J. Smit and H. P. J. Wijn: *Ferrites* (ICON Group International, 1959).
- [75] K. Ando, T. Yoshino, and E. Saitoh: *Applied Physics Letters* **94** (2009).
- [76] F. Czeschka, L. Dreher, M. Brandt, M. Weiler, M. Althammer, I.-M. Imort, G. Reiss, A. Thomas, W. Schoch, W. Limmer, et al.: *Physical Review Letters* **107** (2011) 046601.
- [77] H. Nakayama, K. Ando, K. Harii, T. Yoshino, R. Takahashi, Y. Kajiwara, K.-i. Uchida, Y. Fujikawa, and E. Saitoh: *Physical Review B* **85** (2012) 144408.
- [78] S. Yuasa, T. Nagahama, A. Fukushima, Y. Suzuki, and K. Ando: *Nature Materials* **3** (2004) 868.
- [79] S. Ikeda, J. Hayakawa, Y. Ashizawa, Y. Lee, K. Miura, H. Hasegawa, M. Tsunoda, F. Matsukura, and H. Ohno: *Applied Physics Letters* **93** (2008) 2508.
- [80] T. Miyazaki and N. Tezuka: *Journal of Magnetism and Magnetic Materials* **139** (1995) L231.
- [81] A. Ramirez: *Journal of Physics: Condensed Matter* **9** (1997) 8171.
- [82] D. Hou, Z. Qiu, R. Iguchi, K. Sato, K. Uchida, G. Bauer, and E. Saitoh: *arXiv preprint arXiv:1503.00816* (2015).
- [83] Y.-T. Chen, S. Takahashi, H. Nakayama, M. Althammer, S. T. B. Goennenwein, E. Saitoh, and G. E. W. Bauer: *Journal of Physics: Condensed Matter* **28** (2016) 103004.
- [84] F. J. Dyson: *Physical Review* **98** (1955) 349.
- [85] D.-N. Peligrad, B. Nebendahl, C. Kessler, M. Mehring, A. Dulčić, M. Požek, and D. Paar: *Physical Review B* **58** (1998) 11652.
- [86] K. Kaski, P. Kuivalainen, and T. Stubb: *Journal of Applied Physics* **49** (1978) 1595.
- [87] A. Azevedo, R. Cunha, F. Estrada, O. A. Santos, J. Mendes, L. Vilela-Leao, R. Rodriguez-Suarez, and S. Rezende: *Physical Review B* **92** (2015) 024402.
- [88] C. Ciccarelli, K. M. Hals, A. Irvine, V. Novak, Y. Tserkovnyak, H. Kurebayashi, A. Brataas, and A. Ferguson: *Nature Nanotechnology* **10** (2015) 50.
- [89] D. Wei, M. Obstbaum, M. Ribow, C. H. Back, and G. Woltersdorf: *Nature Communications* **5** (2014).

-
- [90] M. Weiler, J. M. Shaw, H. T. Nembach, and T. J. Silva: *Physical Review Letters* **113** (2014) 157204.
- [91] C. Sandweg, Y. Kajiwara, K. Ando, E. Saitoh, and B. Hillebrands: *Applied Physics Letters* **97** (2010) 252504.
- [92] T. An, K. Yamaguchi, K. Uchida, and E. Saitoh: *Applied Physics Letters* **103** (2013) 052410.
- [93] T. An, V. Vasyuchka, K. Uchida, A. Chumak, K. Yamaguchi, K. Harii, J. Ohe, M. Jungfleisch, Y. Kajiwara, H. Adachi, et al.: *Nature Materials* **12** (2013) 549.
- [94] D. D. Stancil and A. Prabhakar: *Spin waves* (Springer, 2009).
- [95] T. Schneider, A. Serga, T. Neumann, B. Hillebrands, and M. Kostylev: *Physical Review B* **77** (2008) 214411.
- [96] S. Haidar, R. Iguchi, A. Yagmur, J. Lustikova, Y. Shiomi, and E. Saitoh: *Journal of Applied Physics* **117** (2015) 183906.
- [97] A. Ganguly, K. Kondou, H. Sukegawa, S. Mitani, S. Kasai, Y. Niimi, Y. Otani, and A. Barman: *Applied Physics Letters* **104** (2014) 072405.
- [98] R. Iguchi, K. Ando, Z. Qiu, T. An, E. Saitoh, and T. Sato: *Applied Physics Letters* **102** (2013) 022406.
- [99] B. Heinrich, C. Burrowes, E. Montoya, B. Kardasz, E. Girt, Y.-Y. Song, Y. Sun, and M. Wu: *Physical Review Letters* **107** (2011) 066604.
- [100] Y. Sun, Y.-Y. Song, H. Chang, M. Kabatek, M. Jantz, W. Schneider, M. Wu, H. Schultheiss, and A. Hoffmann: *Applied Physics Letters* **101** (2012).
- [101] T. Ishibashi, T. Kosaka, M. Naganuma, and T. Nomura: *Journal of Physics: Conference Series*, Vol. 200, 2010, p. 112002.
- [102] C. H. Du, H. L. Wang, Y. Pu, T. L. Meyer, P. M. Woodward, F. Y. Yang, and P. C. Hammel: *Physical Review Letters* **111** (2013) 247202.
- [103] J. Lustikova, Y. Shiomi, and E. Saitoh: *Physical Review B* **92** (2015) 224436.
- [104] Z. Qiu, M. Uruichi, D. Hou, K. Uchida, H. Yamamoto, and E. Saitoh: *AIP Advances* **5** (2015) 057167.
- [105] A. Tsukahara, Y. Ando, Y. Kitamura, H. Emoto, E. Shikoh, M. P. Delmo, T. Shinjo, and M. Shiraishi: *Physical Review B* **89** (2014) 235317.
- [106] K. Ando, Y. Kajiwara, S. Takahashi, S. Maekawa, K. Takemoto, M. Takatsu, and E. Saitoh: *Physical Review B* **78** (2008) 014413.
- [107] N. Mecking, Y. Gui, and C.-M. Hu: *Physical Review B* **76** (2007) 224430.

-
- [108] A. Yamaguchi, K. Motoi, A. Hirohata, H. Miyajima, Y. Miyashita, and Y. Sanada: *Physical Review B* **78** (2008) 104401.
- [109] H. Kurebayashi, O. Dzyapko, V. E. Demidov, D. Fang, A. Ferguson, and S. O. Demokritov: *Nature Materials* **10** (2011) 660.
- [110] V. Castel, N. Vlietstra, B. van Wees, and J. B. Youssef: *Physical Review B* **86** (2012) 134419.
- [111] K. Harii, T. An, Y. Kajiwara, K. Ando, H. Nakayama, T. Yoshino, and E. Saitoh: *Journal of Applied Physics* **109** (2011) 116105.
- [112] H. Sakimura, T. Tashiro, and K. Ando: *Nature Communications* **5** (2014).
- [113] A. Chumak, V. Vasyuchka, A. Serga, and B. Hillebrands: *Nature Physics* **11** (2015) 453.
- [114] R. Iguchi, K. Ando, R. Takahashi, T. An, E. Saitoh, and T. Sato: *Japanese Journal of Applied Physics* **51** (2012) 103004.